Supporting Information

Aluminum Nanoparticle Enhanced TiO_2 Photocatalysis of Organic Pollutants under Solar and UV-B Irradiation

Saadia Wasim[a], Stephanie Katharine Loeb[*]

[a] Department of Civil Engineering, McGill University, 817 Sherbrooke St W, Montreal, Quebec, Canada, H3A OC3

Number of Pages: 19

Number of Figures: 22

Number of Tables: 2

Number of Texts: 3

Supporting Information includes the following figures, as cross-referenced throughout the main article:

Text S1 - Comparative performance between Ligands

Text S2 – Synthesis of Al Nanoparticles.

Text S3 - Ligand-modified Al/TiO_2 fabrication.

List of Figures:

List of Tables:

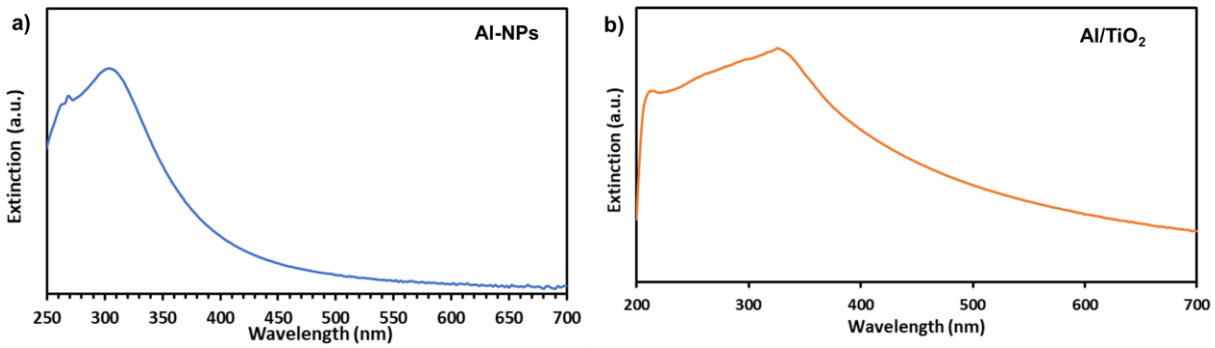

Figure S1. **Absorbance spectra of aluminum nanoparticles and Al/TiO_2 heterostructures.** Ultraviolet–visible absorbance spectra of Al nanoparticles (Al-NPs) dispersed in isopropyl alcohol (IPA) (a) and Al/TiO_2 heterostructures (b).

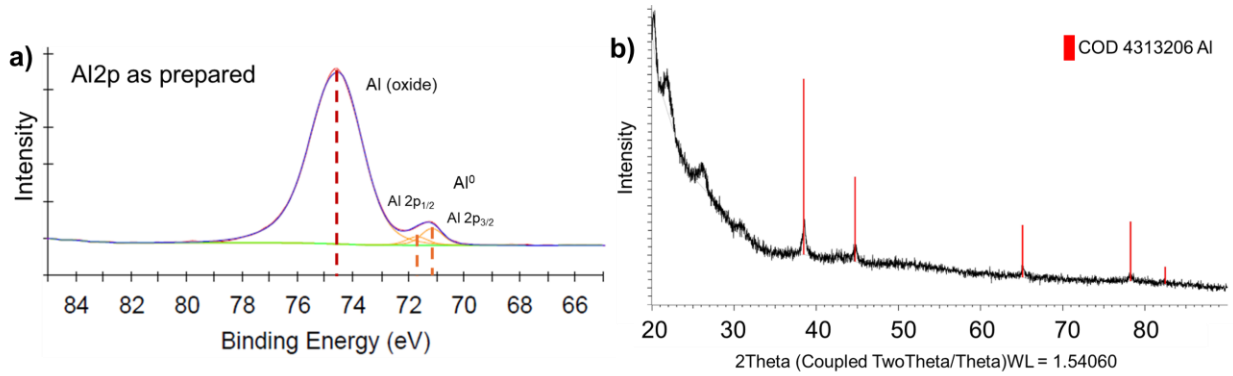

Figure S2. **Structural and chemical characterization of Al nanoparticles (Al-NPs).** X-ray photoelectron spectroscopy (XPS) survey spectrum highlighting the presence of Al 2p signals, with high-resolution Al 2p spectra showing both metallic Al (~71.2 eV) and oxidized Al^{3+} (~74.5 eV), indicating the formation of a thin native oxide shell around the Al cores (a). X-ray diffraction (XRD) pattern showing characteristic reflections of metallic Al (COD no. 4313206), confirming crystalline phase formation; absence of Al_2O_3 peaks indicates the amorphous state of alumina under ambient conditions (b).

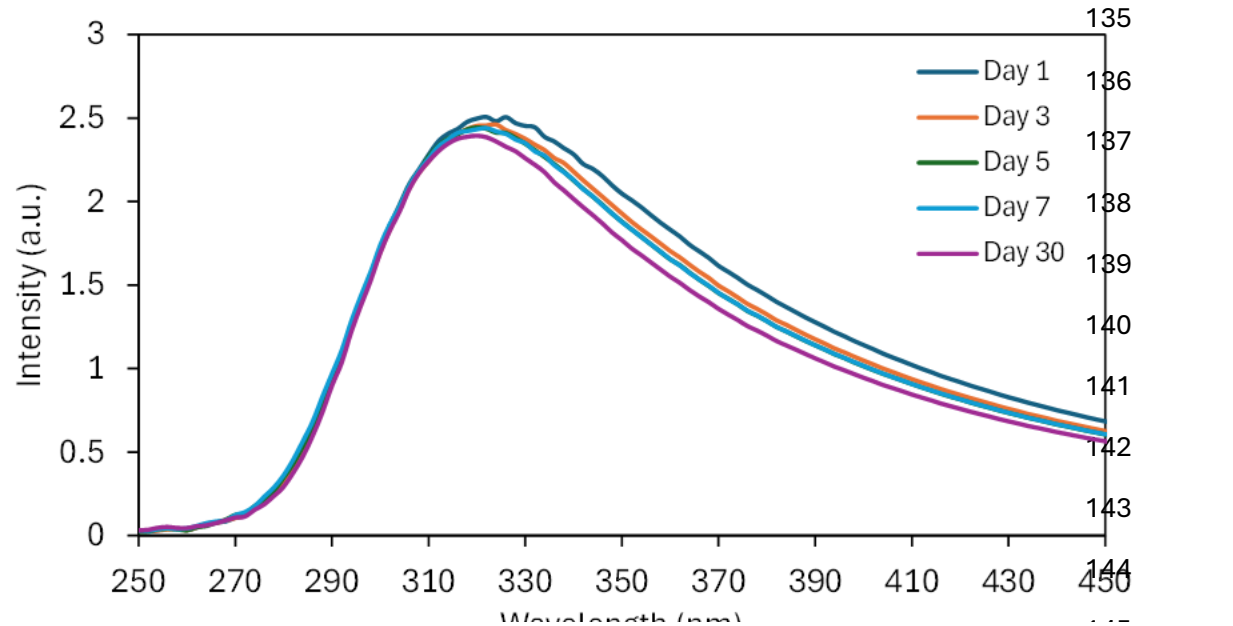

Figure S3. **Time-dependent plasmonic absorbance of Al nanoparticles in the UV region.** Ultraviolet (UV) absorbance spectra of Al nanoparticles (Al-NPs) recorded at different time intervals, showing the evolution of plasmonic properties over time.

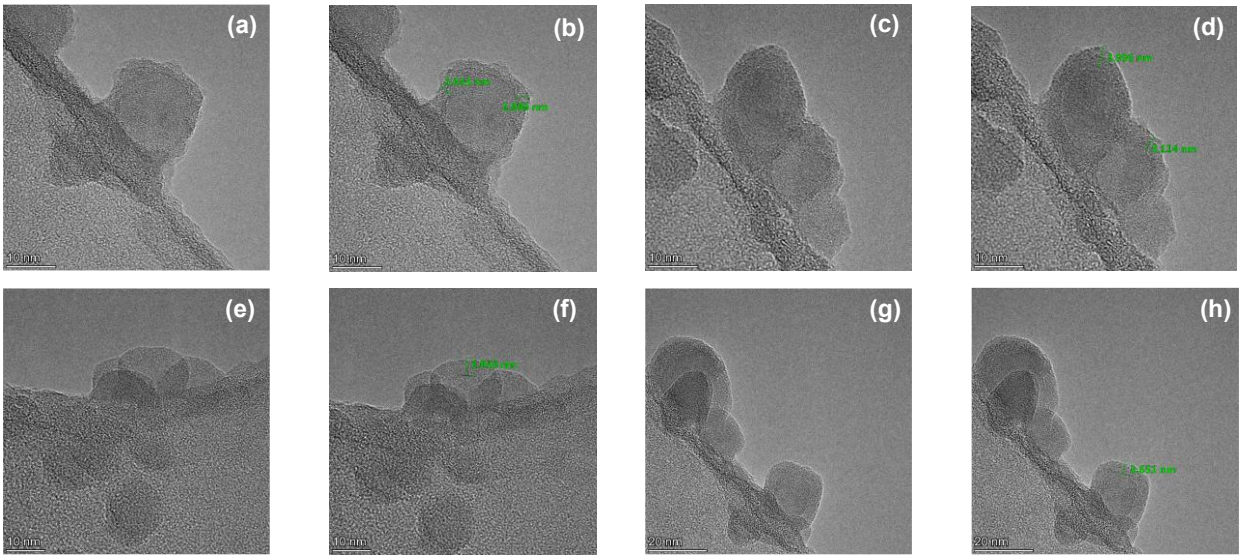

Figure S4. **High-resolution transmission electron microscopy (HRTEM) images of Al-NP cores and Al_2O_3 shells.** HRTEM images showing the Al nanoparticle cores and their native Al_2O_3 shells with measured dimensions (a–h). Scale bars: 10 nm (a–f) and 20 nm (g–h).

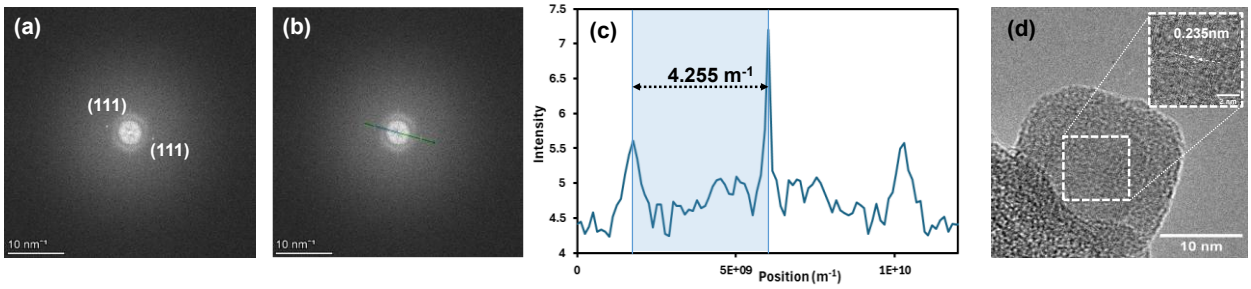

Figure S5. **Diffraction analysis of Al nanoparticles (Al-NPs).** Diffraction patterns of Al-NPs showing the origin (000) and the (111) planes with (a) and without (b) measurement lines. Intensity profile extrapolated from the diffraction pattern for calculating the reciprocal interplanar distance (4.255 nm^{-1}), corresponding to an interplanar spacing of 0.235 nm (c). The crystallinity of the synthesized Al-NPs was determined to be 71.4% based on X-ray diffraction (XRD) analysis.

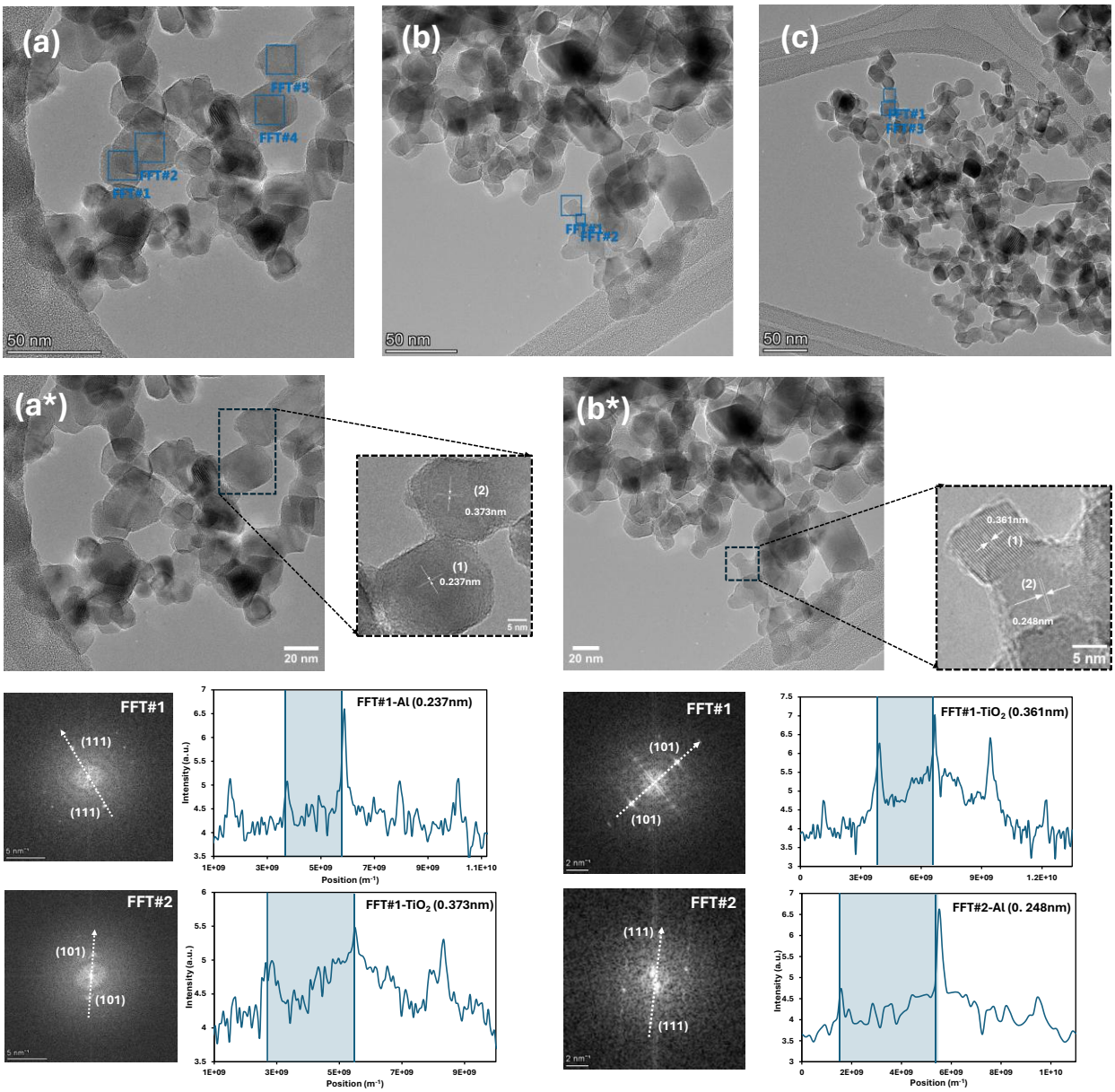

Figure S6. **Transmission electron microscopy (TEM) characterization of Al/TiO_2 Cys.** TEM images of Al/TiO_2 Cys heterostructures with corresponding fast Fourier transform (FFT) analysis (a–c). High-resolution TEM (HRTEM) images of panels a and b showing interplanar distances for Al nanoparticles and P25 TiO_2 (a*–b*).

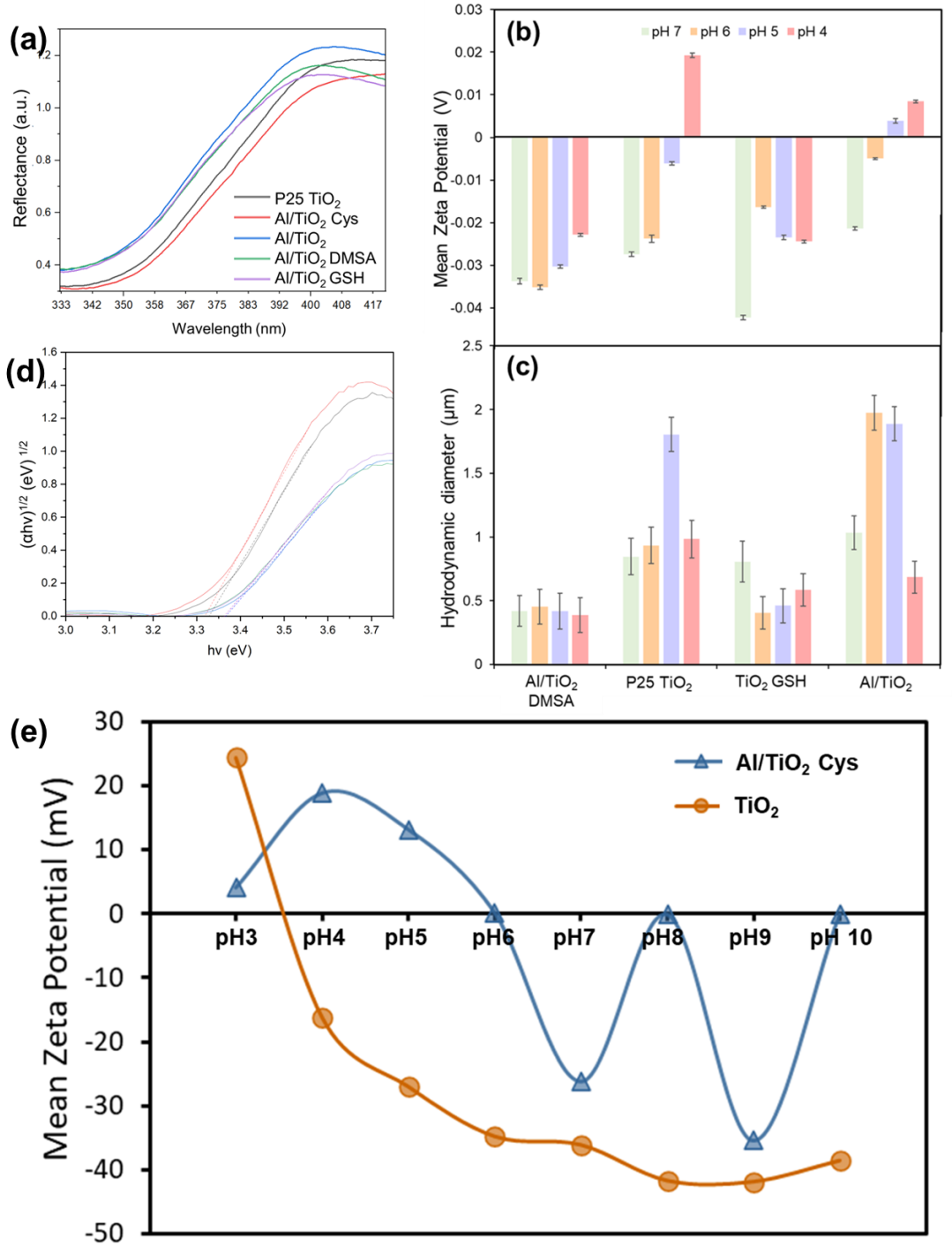

Figure S7. **Optical and physicochemical characterization of ligand-modified Al/TiO_2 heterostructures and TiO_2 references.** Reflectance spectra as a function of wavelength for Al/TiO_2 heterostructures modified with cysteine (Cys), glutathione (GSH), or dimercaptosuccinic acid (DMSA), Al/TiO_2, Cys-modified TiO_2, and P25 TiO_2 (a). Tauc plots used to estimate bandgap energies (sample concentration: 1000

ppm, 3 mL) (b). Surface charge (zeta potential) and hydrodynamic size of nanoparticles measured at pH 4-7 and a concentration of 0.003 w/v % (c-d). Isoelectric point of Al/TiO_2 Cys and P25 TiO_2 determined by titration (e).

Table S1. Characterization of various ligand-modified Al/TiO_2 heterostructures, non-ligand modification and P25 TiO_2

Sample	BET specific surface area m^2/g	Pore diameter (nm)	Eg (eV)	ZetaPotential (V)	Z-Ave d (nm)	Polydispersity index (PDI)
P25 TiO_2	49.3	28.75	3.27	-15	222.16	0.17
Al/TiO_2 Cys	44	36	3.27	51	404.79	0.38
Al/TiO_2 DMSA	39	36	3.32	-12	1675.82	0.37
Al/TiO_2 GSH	53	36	3.32	30	1655.47	0.4
Al/TiO_2	47.43	36	3.32	45	387.92	0.37

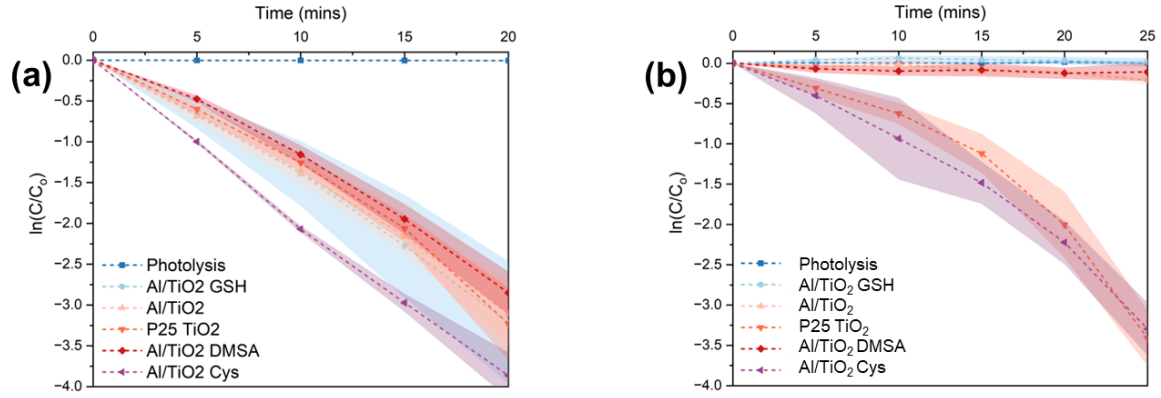

Figure S8. **Photocatalytic degradation of amaranth and phenol under broadband UV-B irradiation using ligand-modified Al/TiO_2 heterostructures.** Degradation of amaranth (C_0 = 20 ppm, 20 min) and phenol (C_0 = 10 ppm, 25 min) under broadband UV-B (280-320 nm, 14.6 W m^{-2}) using different ligand-modified Al/TiO_2 heterostructures.

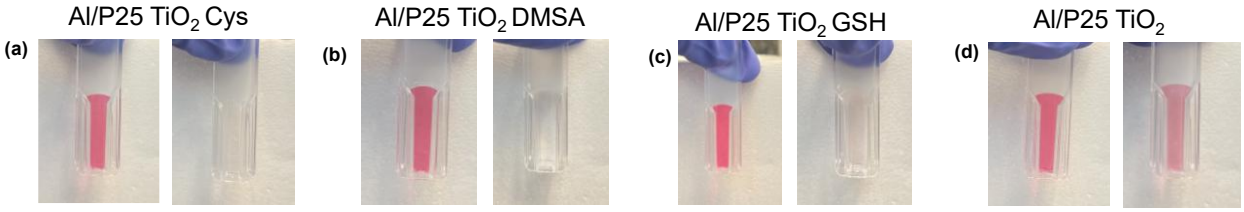

Figure S9. **Photographs showing amaranth colour change during photocatalytic degradation using nanoparticles under broadband UV-B irradiation.** Images of amaranth (C_0 = 20 ppm)

recorded from the start to the end of the experiment for each nanoparticle sample under broadband UV-B (280-320 nm, 14.6 W m^{-2}).

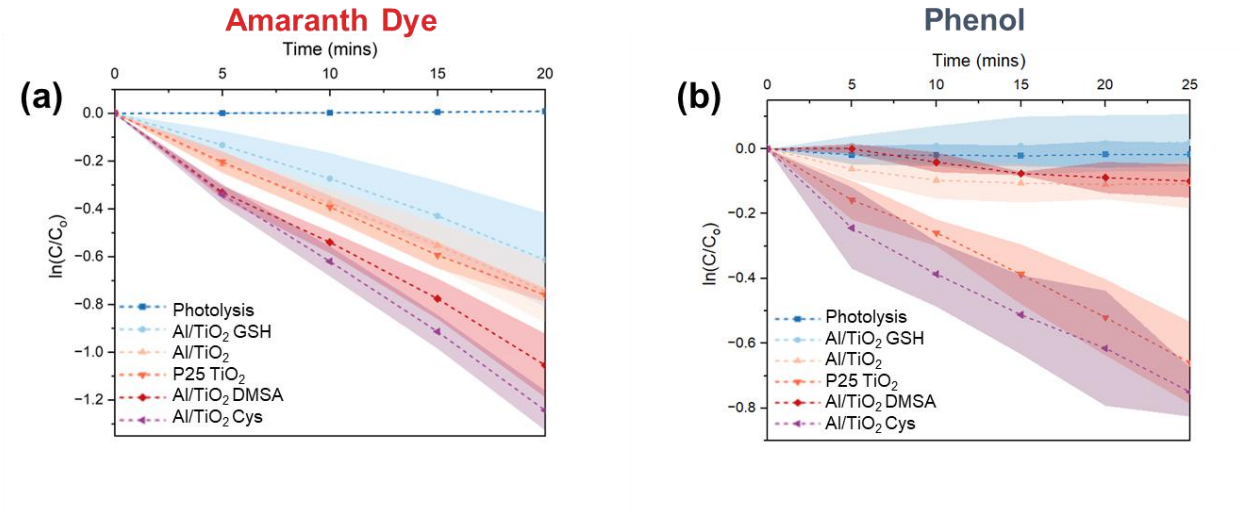

Figure S10. **Photocatalytic degradation of amaranth and phenol under simulated solar irradiation using ligand-modified Al/TiO_2 heterostructures.** Degradation of amaranth (C_0 = 20 ppm, 20 min) and phenol (C_0 = 10 ppm, 25 min) using different ligand-modified Al/TiO_2 heterostructures under simulated solar irradiation (with a UVC filter blocking UV light < 280 nm; irradiance: 286.26 W m^{-2}).

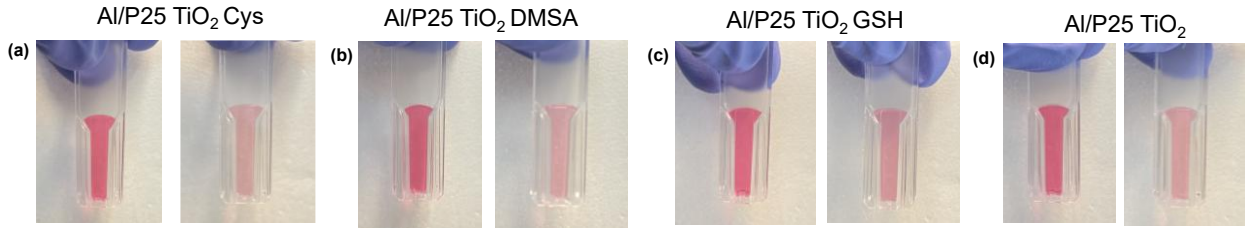

Figure S11. **Photographs showing amaranth colour change during photocatalytic degradation under simulated solar irradiation.** Images of amaranth (C_0 = 20 ppm) recorded from the start to the end of the experiment for each

nanoparticle sample under simulated solar irradiation (with a UVC filter blocking UV light < 280 nm; irradiance: 286.26 W m^{-2}).

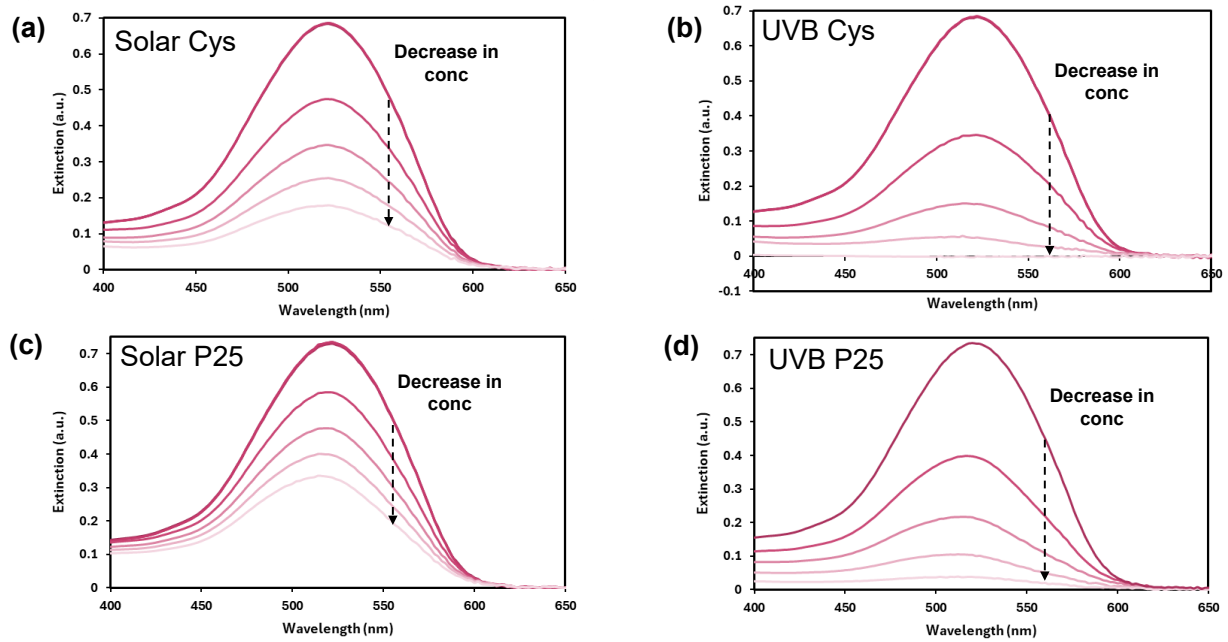

Figure S12. **UV-vis spectra showing photocatalytic degradation of amaranth using Al/TiO_2 Cys and P25 TiO_2.** UV-vis absorbance spectra of amaranth (C_0 = 20 ppm) recorded during photocatalytic degradation under simulated solar irradiation (with a UVC filter blocking UV light < 280 nm; irradiance: 286.26 W m^{-2}) and broadband UV-B (280-320 nm, 14.6 W m^{-2}). Panels a-b show spectra for Al/TiO_2 Cys, and panels c-d show spectra for P25 TiO_2.

Text S1. Comparative performance between Ligands: The photocatalytic performance of Al/TiO_2 heterostructures was evaluated, with Al/TiO_2 Cys demonstrating superior degradation of amaranth and phenol compared to other ligand-modified and non-modified Al/TiO_2 heterostructures. The degradation of both contaminants followed a first-order kinetic model, with high correlation coefficients (R^2 > 0.99 for UV-B and >0.90 for solar irradiation). Under solar irradiation, Al/TiO_2 Cys achieved a 71% reduction in amaranth concentration after 20 minutes and a 53% reduction in phenol after 25 minutes, outperforming P25 TiO_2 by 60% for amaranth

degradation and 10.5% for phenol degradation. In contrast, other ligand-modified Al/TiO_2 heterostructures exhibited lower efficiency, with Al/TiO_2 GSH showing particularly poor performance, as shown in SI Fig. S13. The 60% enhancement of Al/TiO_2 Cys compared to the benchmark P25 TiO_2 under simulated sunlight was calculated using the rate constants in the following formula:

$$\% \, enhancement = \frac{v_{Al\,TiO2\,Cys} - v_{TiO2}}{v_{TiO2}} * 100$$

Under UV-B irradiation, Al/TiO_2 Cys again outperformed P25 TiO_2, achieving 98% amaranth degradation after 20 minutes, while performing similarly to P25 TiO_2 in phenol degradation. Other ligand-modified Al/TiO_2 heterostructures showed comparable degradation to P25 TiO_2 for amaranth but negligible degradation for phenol. Cys exhibits stronger coordination with the Al/Al_2O_3 core through its -SH group and with P25 TiO_2 via -NH_2 and -COOH functional groups, as confirmed by ATR-FTIR analysis. Compared to DMSA and GSH, this dual binding enhances the structural stability and facilitates more efficient charge transfer across the Al/TiO_2 interface, leading to improved photocatalytic performance of Al/TiO_2 Cys, particularly toward anionic contaminants.

Table S2. Degradation performance of various ligand-modified Al/TiO_2 heterostructures, non-ligand modification and P25 TiO_2

	% Degradation-UVB		% Degradation-Solar		k-value (min^{-1}) UVB Degradation		k-value (min^{-1}) Solar Degradation	
Sample	Amaranth	Phenol	Amaranth	Phenol	Amaranth	Phenol	Amaranth	Phenol
P25 TiO_2	95.4	99.8	53	49.5	0.1584	0.1293	0.0382	0.0258
Al/TiO_2 Cys	98	96.2	71	53	0.1998	0.1285	0.0612	0.0285
Al/TiO_2 DMSA	94	10	65	9.4	0.1434	0.0039	0.0511	0.0046
Al/TiO_2 GSH	95	-1.3	45	-2.2	0.1608	0.00008	0.0305	0.0008
TiO_2 Cys	92.5	58.7	49.5	21.9	0.132	0.0371	0.0343	0.0098
Al/TiO_2	95.3	18.9	52	10	0.1537	0.0076	0.0366	0.0039

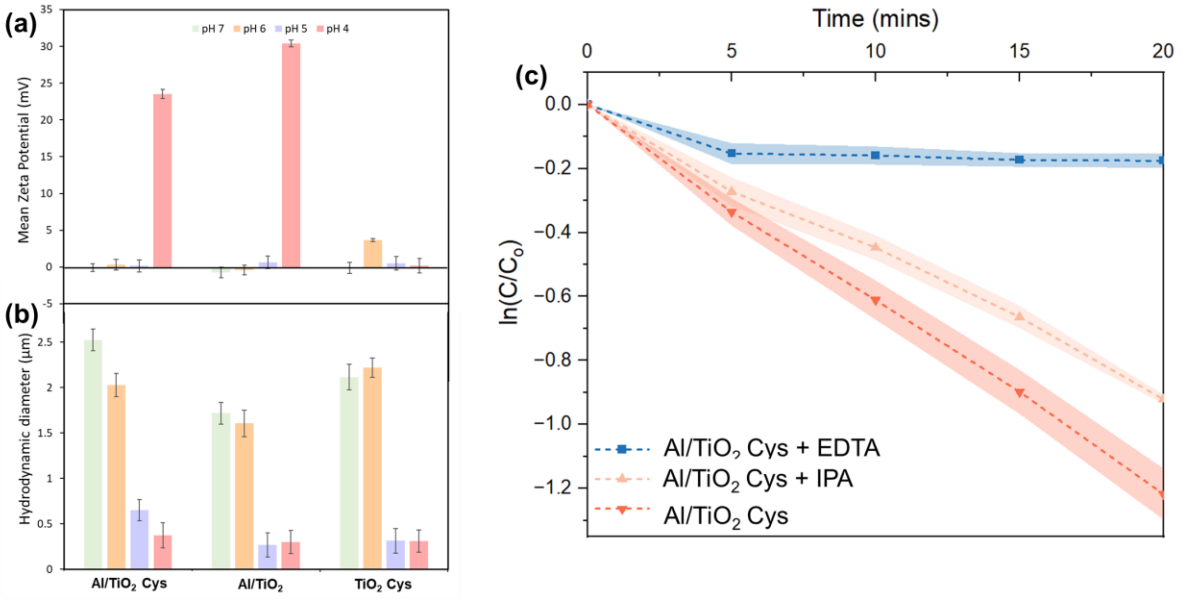

Figure S13. **Physicochemical characterization of Al/TiO_2 Cys, Al/TiO_2, and Cys-modified TiO_2 to evaluate the effect of phenol on aggregation.** Phase analysis light scattering (PALS) measurements (a), dynamic light scattering (DLS) size distribution (b), and scavenging experiments performed using 10 mM EDTA and 100 mM isopropyl alcohol (IPA) (c).

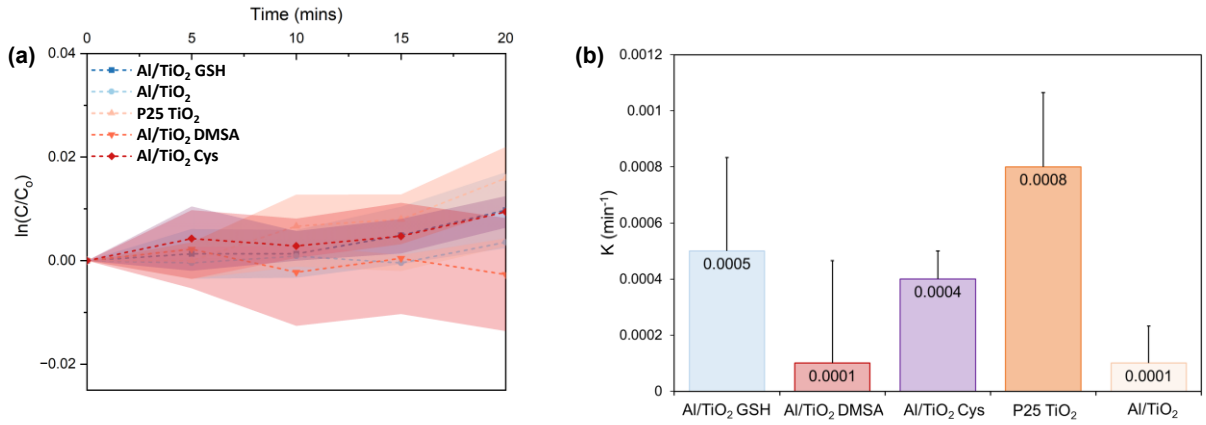

Figure S14. **Dark control experiment for amaranth degradation.** Photocatalytic degradation of amaranth (C_0 = 20 ppm) monitored under dark conditions at room temperature.

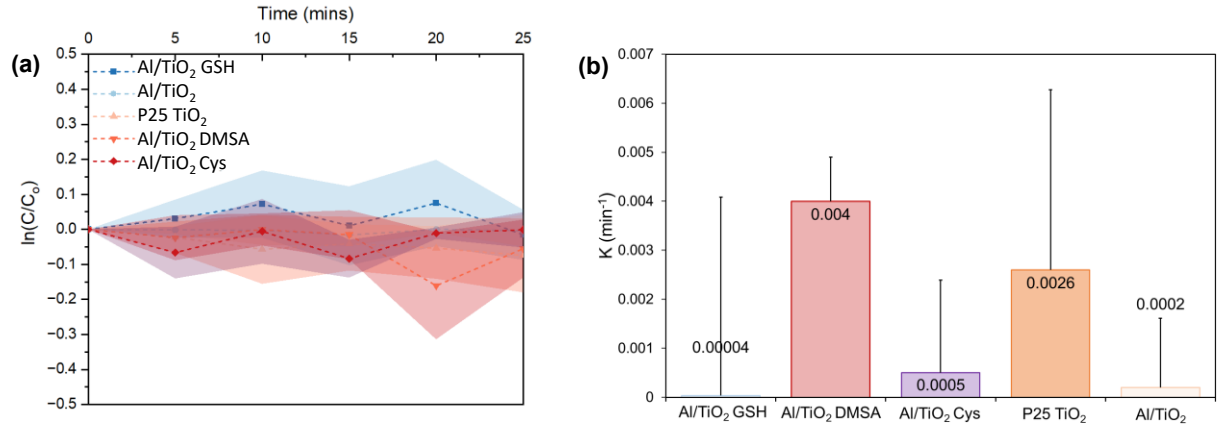

Figure S15. **Dark control experiment for phenol degradation.** Photocatalytic degradation of phenol (C_0 = 10 ppm) monitored under dark conditions at room temperature.

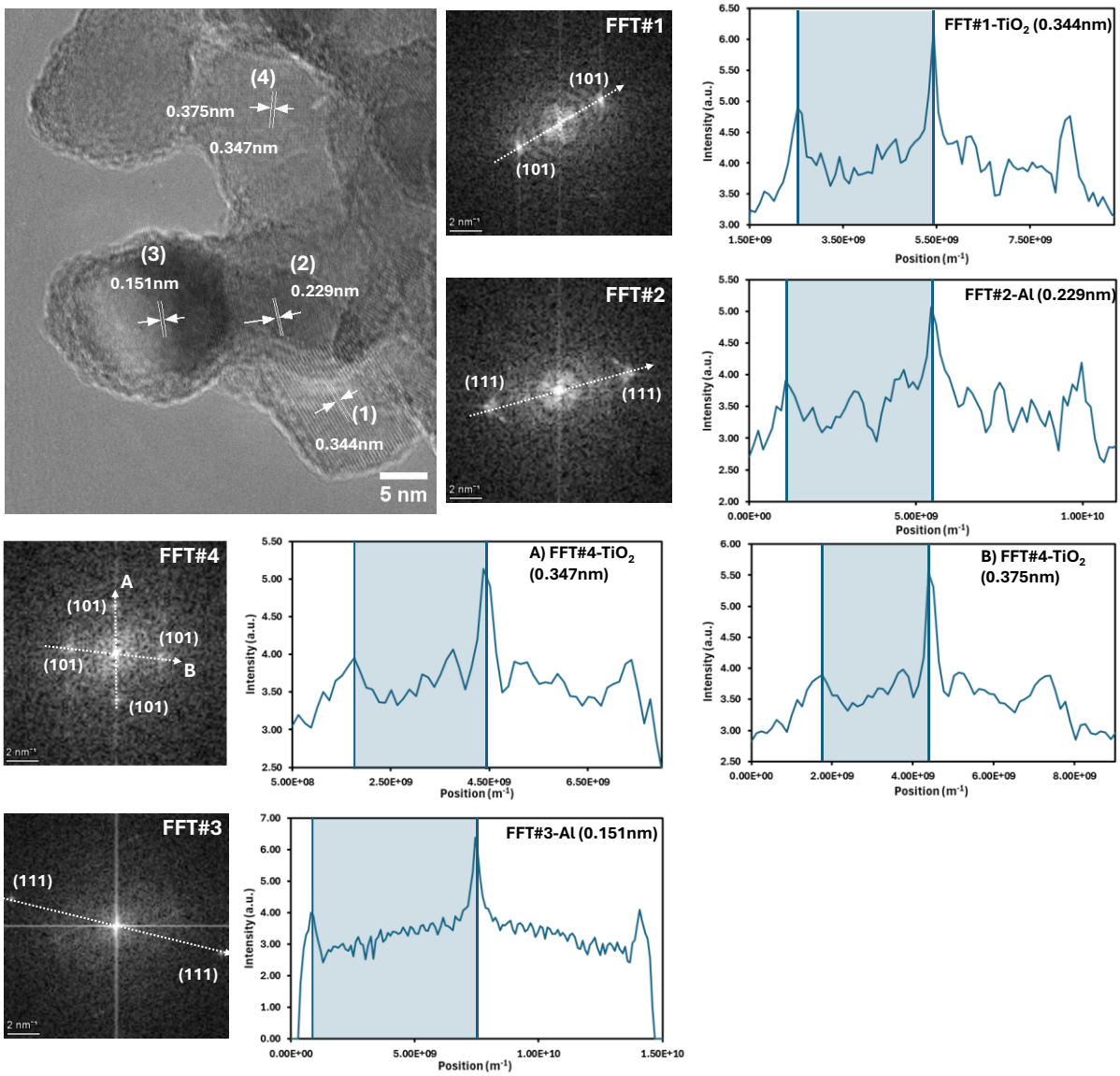

Figure S16. **HRTEM characterization and photocatalytic degradation of amaranth using Al/TiO_2 Cys and P25 TiO_2.** High-resolution transmission electron microscopy (HRTEM) images showing interplanar distances for Al nanoparticles (0.151 nm and 0.229 nm) and P25 TiO_2 (0.344 nm and 0.347 nm) at the start of the experiment. Diffraction patterns were used to calculate the reciprocal of the interplanar distances from intensity versus position graphs. Photocatalytic degradation of amaranth (C_0 = 20 ppm) was performed for 20 min under simulated solar irradiation with a UVC filter blocking UV light < 280 nm (irradiance: 286.26 W m^{-2}).

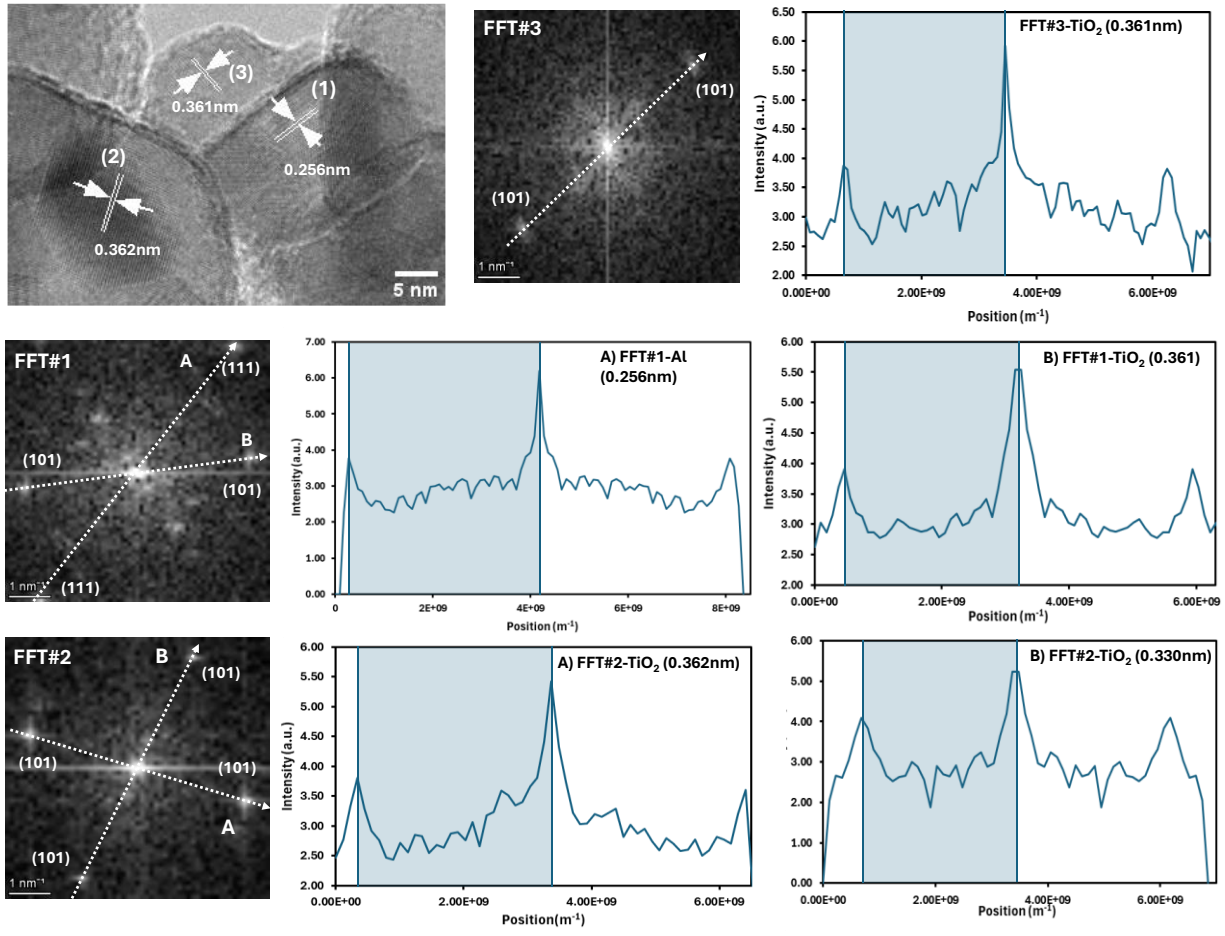

Figure S17. **HRTEM characterization and photocatalytic performance of Al-NPs and P25 TiO_2.** High-resolution transmission electron microscopy (HRTEM) images of (a) Al nanoparticles (Al-NPs) and (b) P25 TiO_2 collected at the end of the experiment, showing interplanar distances of 0.256 nm for Al-NPs and 0.362/0.361 nm for P25 TiO_2. Insets: corresponding selected area electron diffraction (SAED) patterns, with inverse interplanar distances calculated from intensity

versus position plots. (c) Photocatalytic degradation of Amaranth dye (initial concentration 20 ppm) under solar irradiation (286.26 W m^{-2}) for 20 minutes using a UVC filter to block wavelengths below 280 nm.

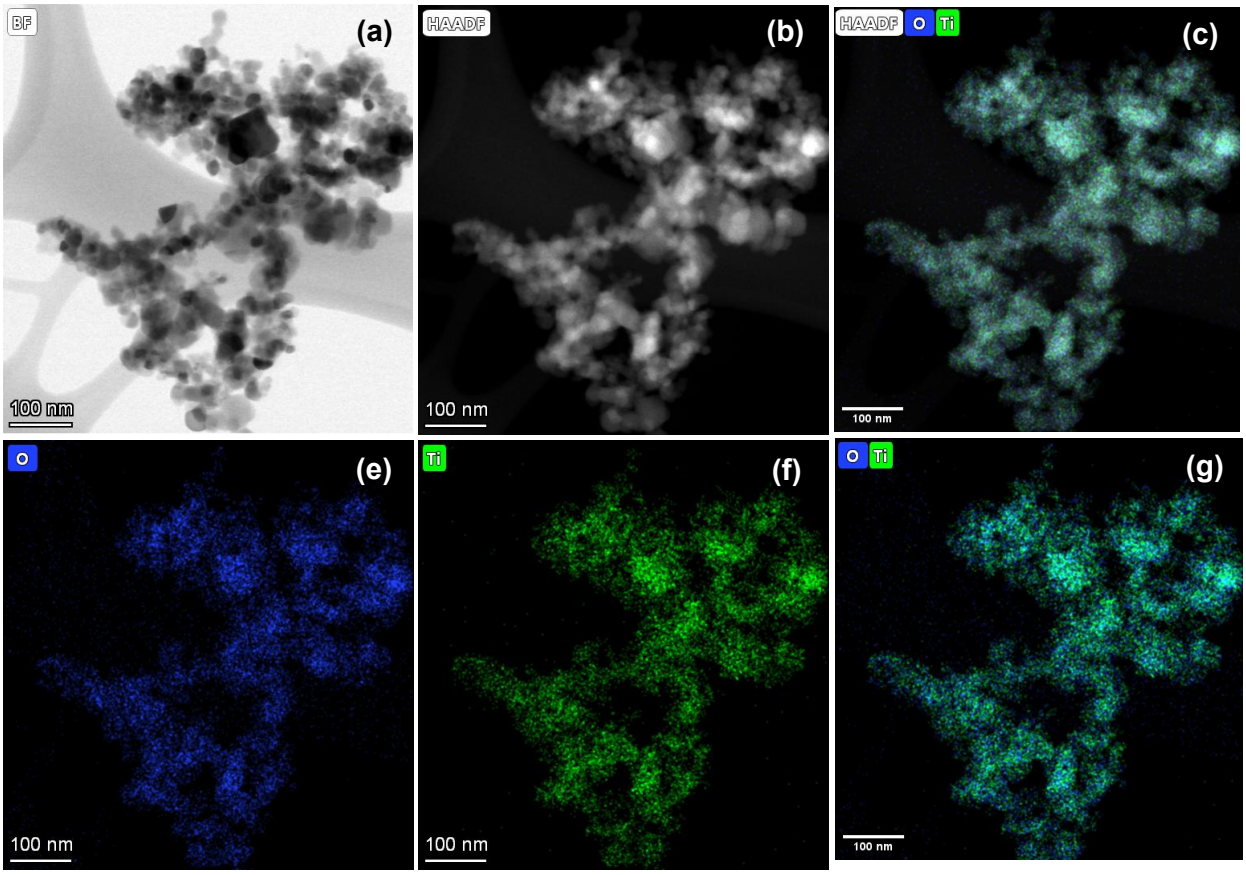

Figure S18. **Electron microscopy of P25 TiO_2.** High-angle annular dark-field (HAADF), bright-field (BF), and scanning transmission electron microscopy (STEM) images of P25 TiO_2 nanoparticles. Scale bar: 100 nm.

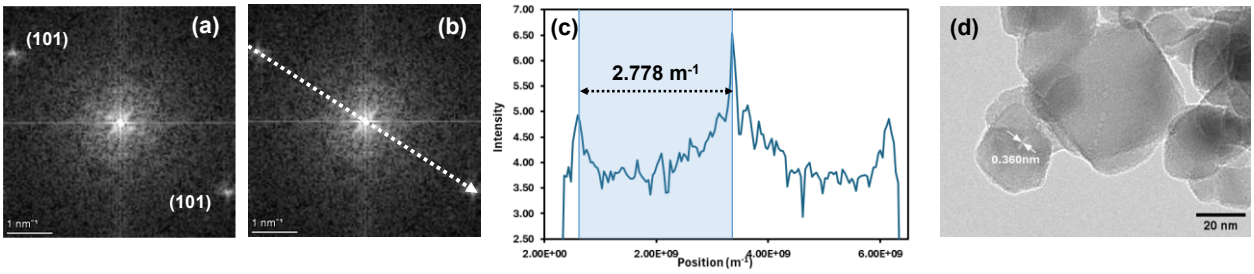

Figure S19. **X-ray diffraction analysis of P25 TiO_2.** Diffraction patterns of P25 TiO_2 showing the origin (000) and the (101) lattice planes, with one panel including a measurement line for reference. An intensity profile extracted from the diffraction pattern was used to calculate the reciprocal interplanar distance (2.778 nm^{-1}) and the corresponding interplanar spacing (0.360 nm). XRD analysis indicates a crystallinity of 74% for P25 TiO_2.

Text S2. Synthesis of Al Nanoparticles. Aluminum nanoparticles were synthesized in an inert environment using the Schlenk line protocol[1]. Nanoparticles were synthesized by the addition of 24 mL of degassed trioctylphosphine in an argon purged Schlenk flask followed by heating at 60°C with vigorous stirring using a metallic block. Next, 6 mL of N, N-dimethylethylamine alane - DMEAA (0.5M in toluene) was added and allowed to stir for 5 minutes. Then, 1.5 mL of Titanium (IV) isopropoxide- TIP (50 mM in toluene) was added to catalyze the decomposition of alane into metallic Al. The reaction mixture turns into a dark, translucent brown color upon the addition of TIP, which gradually changes to an opaque black suspension, indicating the formation of small Al NCs. The reaction was then left to stir for 4 hours at 60 °C under argon flow. Lastly, 10 mL of dibutyl phosphate (50 mM in cyclohexane) was added to end the process. The flask was then opened to air, resulting in the formation of a 3-5 nm, self-limiting, amorphous Al_2O_3 layer at the particle surface. This oxide layer prevents further oxidation of the underlying Al core by air. The nanoparticles were collected through multiple rounds of centrifugation and resuspension in isopropanol. To remove aggregates or large particles, the sample was ultracentrifuged up to 4 times at 10,000xg for 10 mins. For the first 3 washes, the supernatant was discarded, leaving behind the pellet, and for the last wash, the supernatant was collected and diluted for the fabrication of the heterostructures as mentioned in the methods section. UV absorbance characterization of the Al-NPs was performed, and a peak in the UV region was observed. The position and width of the peak varied for each synthesis; however, the absorbance was in the UV region. This could probably be attributed to the size of the nanoparticles in the supernatant from the final centrifuge.

Text S3. Ligand-modified Al/TiO_2 fabrication. Ligands were weighted, 0.01 g of both GSH and DMSA and 0.006 g of Cys, and added to 5 mL of Al-NPs (of conc 67-70 µg/L). The mixture was sonicated for 10 minutes and mixed for 30 minutes. The supernatant was separated from any unmixed ligands, such as Cys, by pouring the supernatant into a different Falcon tube for the next step of the fabrication. 20 mg of P25 TiO_2 was added to the suspension and sonicated for 10 mins, followed by mixing for 30 mins. Following this step, centrifugation was performed to separate the pellet and supernatant.

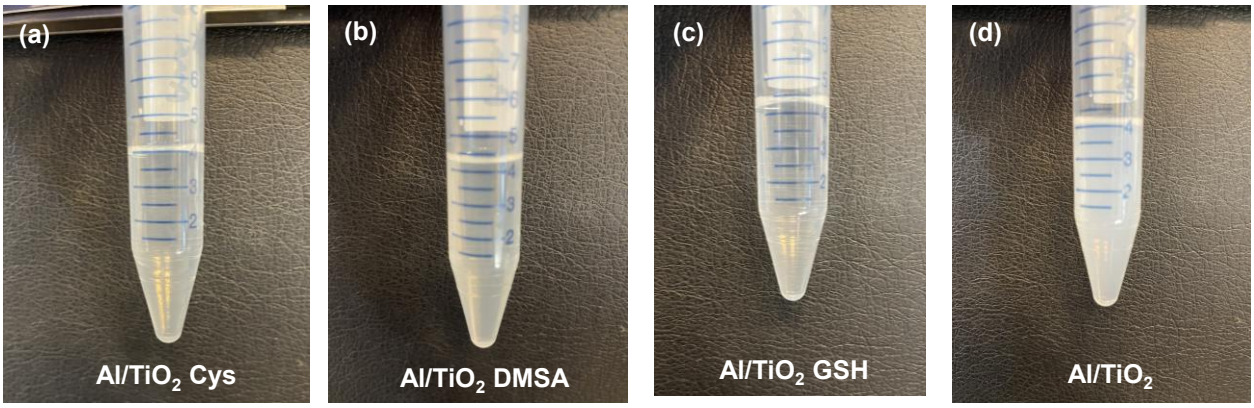

Figure S20. **IPA supernatant after centrifugation of ligand-modified and unmodified Al/TiO_2 heterostructures.** (a-c) Transparent supernatant from suspensions with ligands, indicating stabilized interactions and effective binding between Al nanoparticles and P25 TiO_2 nanoparticles. (d) Opaque supernatant from suspensions without ligands, showing lack of binding between Al and P25 TiO_2 nanoparticles.

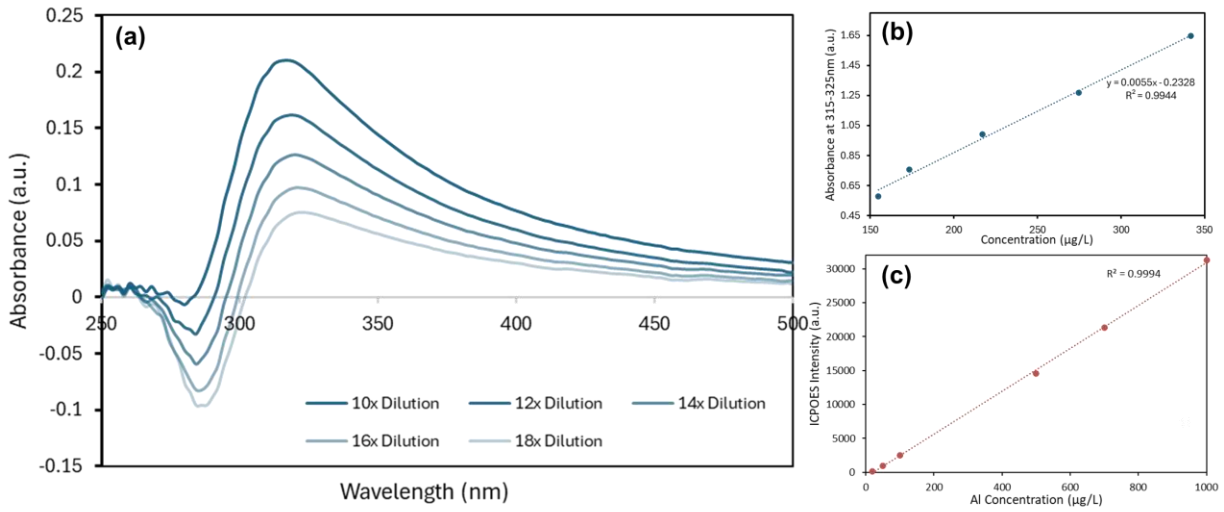

Figure S21. **Calibration of Al nanoparticle mass using UV-vis spectrophotometry and ICP-OES.** (a) UV-vis calibration curve for synthesized Al nanoparticles. (b) Relationship between absorbance and concentration determined from the area under the UV-vis spectra between 315-325 nm. (c) ICP-OES calibration curve for Al dilution samples measured at the 394.401 nm emission line, using QC 4 as Al standards. Data from ICP-OES were used to validate and calibrate the UV-vis measurements for mass determination of Al nanoparticles.

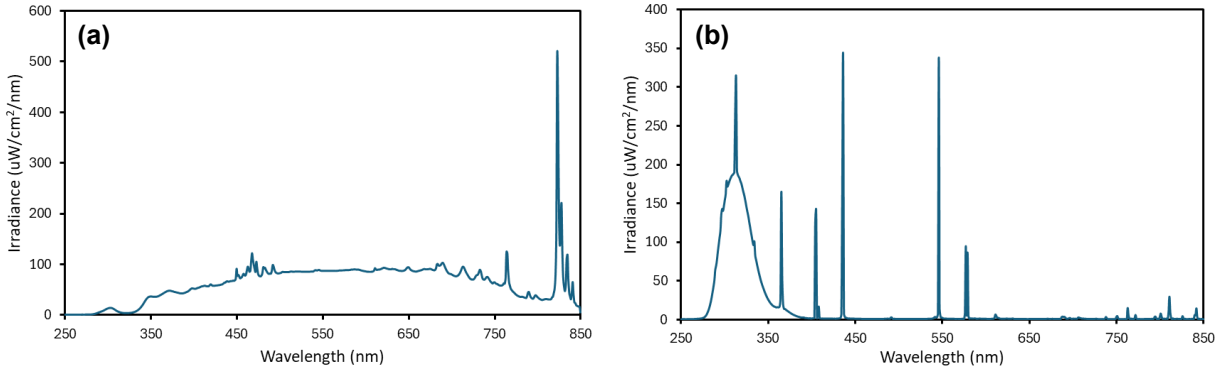

Figure S22. **Irradiation spectra of the light source measured with a radiometer.** (a) Solar spectrum recorded with a UVC filter (<280 nm) showing an intensity of 286.26 W m^{-2}. (b) Broadband UVB spectrum (280-320 nm) with an intensity of 14.6 W m^{-2}.

References:

1 Bayles, A. *et al.* Al@TiO2 Core-Shell Nanoparticles for Plasmonic Photocatalysis. *ACS Nano* (2022). https://doi.org:10.1021/ACSNANO.1C10995

325